

# Automatic Pupillometry From Digital Images

D. Robert Iskander\*, *Member, IEEE*, Michael J. Collins, Siegfried Mioschek, and Martin Trunk, *Member, IEEE*

**Abstract**—Determination of two-dimensional characteristics of the anterior surface of the eye is becoming increasingly important in modern optometry and ophthalmology practice. In particular, accurate estimation of the pupil size and centration is crucial in customized refractive surgery, corneal transplantation, and advanced contact lens fitting. The pupil parameters change under different lighting conditions so they often need to be related to some fixed reference such as the limbus outline. However, current commercial pupillometers do not estimate limbus position. We present a novel algorithm for automatic extraction of pupil parameters from digital images that takes the relative limbus information into account. The algorithm utilizes several customized image processing techniques that form a robust procedure which performs well for a wide range of clinical images. We apply the developed algorithm to images obtained by a standard digital camera, and specialized ophthalmic instruments such as a wave-front sensor and a high-speed imaging system.

**Index Terms**—Eye biometrics, limbus, pupil.

## I. INTRODUCTION

**P**UPILLOMETRY is essentially concerned with the measurement of two important geometrical characteristics of the pupil: pupil size and pupil location with respect to other anatomical structures of the eye. In general, pupil size determines the amount of light falling on the retina and defines the optical characteristics of the eye [1]. The center of the pupil is close to the major optical axis and decentration is responsible for asymmetries in the optical system of the eye. It is well known that the pupil changes its size under different lighting conditions. These changes, however, are not concentric. With changes in pupil dimension the pupil center often moves in relation to other ocular landmarks [2].

For some time vision researchers have been interested in the magnitude and direction of changes of the pupil center for different light conditions. A significant shift of the pupil center of up to 0.7 mm has been observed for dilated pupils [3]. Other

sources report smaller shifts from 0.4 to 0.5 mm [2], [4]. It has also been found that the alternations in the pupil centration are not regular across the population.

Recently, an accurate measurement of pupil size and center has become increasingly important in keratorefractive procedures, such as laser in situ keratomileusis (LASIK) surgery, where it has a profound effect on the predicted outcome of the procedure [5], [6]. It may also determine whether a patient is suitable for refractive surgery [7]. Another aspect of pupillometry in refractive surgical correction arises in the area of eye-tracking [8], [9]. Eye trackers are being routinely used in customized refractive surgery where the output of an eye-tracking system is used for control of a corneal laser ablation pattern. Other medical applications of accurate pupillometry include monitoring sleep patterns in hypersomnolent patients [10], the reaction of pupils to light in psychophysiological analysis [11], and forensic medicine [12].

The growing interest in customized refractive surgeries is not the only factor that drives the need for improved pupillometry. Current advances in soft contact lens correction and human corneal transplantation place a significant demand on eye biometrics in general and particularly on the determination of pupil parameters. For example, in a bifocal contact lens fitting, the relation between corneal apex, the pupil center, and the limbus center will influence the lens position on the eye [13]. Also, the relation between the center of the pupil and the center of the limbus is crucial in corneal transplantation where the centration of the corneal graft relative to the pupil and limbus centers, or the point of the greatest corneal curvature, has to be established [14], [15].

Several commercial pupillometers exist. They range from specially designed rulers or gauges to highly sophisticated infrared video-based systems. Over the last few years several studies of accuracy and reliability of popular pupillometers have been conducted [16]–[19]. As noted in [6], using gauges we can estimate the pupil diameter with  $\pm 1$  mm accuracy. Infrared tube-based pupillometers are more accurate than the gauges. They often provide a digital read out of pupil size to  $\pm 0.5$  mm. Most accurate systems are based on objective infrared video systems with accuracy of about  $\pm 0.1$  mm. Comparison between these instruments show that the final result depends to a large extent on the technical experience of the person performing the measurement. Pupil parameters can also be estimated with a videokeratoscope, an instrument primarily used for measuring corneal elevation [20]. However, the accuracy of this methodology has been questioned for eyes with dark irides [21].

There is one common deficiency in current pupillometers that they do not measure the location of the pupil center in reference to the corneal limbus. As a consequence, measurement of

Manuscript received August 8, 2003; December 21, 2003. The work was supported by the QUT Strategic Collaborative Program scheme. *Asterisk indicates corresponding author.*

\*D. R. Iskander is with the Contact Lens and Visual Optics Laboratory, School of Optometry, Queensland University of Technology, Kelvin Grove Q4059, Brisbane, Australia (e-mail: d.iskander@qut.edu.au).

M. J. Collins is with the Contact Lens and Visual Optics Laboratory, School of Optometry, Queensland University of Technology, Kelvin Grove Q4059, Brisbane, Australia (e-mail: m.collins@qut.edu.au).

S. Mioschek was with the Contact Lens and Visual Optics Laboratory, School of Optometry, Queensland University of Technology, Kelvin Grove Q4059, Brisbane, Australia, and also with the School of Electronics, Carinthia Tech Institute, Villach 9524, Austria.

M. Trunk was with the Contact Lens and Visual Optics Laboratory, School of Optometry, Queensland University of Technology, Kelvin Grove Q4059, Brisbane Australia and also with the School of Electronics, Carinthia Tech Institute, Villach 9524, Austria. He is now with Byometric Systems GmbH, Mitterfelden D-83404, Germany.

Digital Object Identifier 10.1109/TBME.2004.827546



the image is not uniformly sharp due to small depth of focus typical for macro photography.

Gray-scale images are used in the procedure. Although, in many digital image processing applications there is a need to adjust image brightness, perform sharpening transformation or histogram equalization, none of such techniques is used in our algorithm. In other words, all images used in the proposed automatic pupillometry procedure contain original raw information.

The next step in the image acquisition is to determine the initial origin of the  $XY$  axes. We choose the approximate center of the pupil for this purpose. Finding pupil in the image can be achieved in several ways. Typically, it is assumed that the pupil location corresponds to an image area with low intensity. However, techniques based on this assumption often fail when the image contains regions of dark hair or other dark features. In [30], we have presented a robust and fast technique for finding the pupil center in the image using a detector based on quadruple axes symmetry indicator (QSI). More sophisticated techniques are available, including methods based on multiple light sources [31] and curvature algorithms [32].

The initial origin  $(x_0^{(0)}, y_0^{(0)})$ , where the superscript denotes the iteration step, is determined either by applying the QSI detector and cropping the image using the reference scale, or simply by choosing the geometrical center of the image, as is the case for images from a wavefront sensor or a high-speed camera.

The next step in the procedure is to set the initial limbus sectors. We define a limbus sector as an image area where the transition from the iris to the sclera is clearly visible. Thus, the limbus sectors depend on the characteristics of the individual eye and its direction of gaze. In the natural gaze position, for example, the initial limbus areas could be set between  $-5\pi/18$  and  $2\pi/9$  for the right-hand side of the image and between  $7\pi/9$  and  $-13\pi/18$  for the left-hand side, as depicted in Fig. 3. It could be argued that these two limbus sectors should be different for left and right eyes or for Caucasian versus Asian eyes, because of the normal differences in lid position and angle. Thus, auxiliary information on the particular type of image can be always included to determine the initial limbus sectors that are used. One important aspect of setting limbus sectors is the position of the eyelids. For example, during a down gaze or a blink, the limbus sectors have to be updated. When a sequence of images is available from a video stream, the algorithm updates the limbus sectors for every frame ensuring that there is sufficient data from which limbus outline can be extracted.

After selecting the initial limbus sectors, we can proceed with the detection of the limbus outline. First, the data inside each of the limbus sectors is transformed from Cartesian to polar coordinates. There are several ways such transformation can be performed [22]. Since this is not a critical step in the procedure, one may choose to sample the data for a given discrete angular and radial set of coordinates using, for example, nearest neighbor or bilinear interpolation. The sampled data from the two limbus sectors form two polar coordinate images as shown in Fig. 4(a) and (b). First, all radial profiles are averaged across the limbus sector to find the trend in the image intensity. It is expected that an average intensity profile has a clear transition from the darker

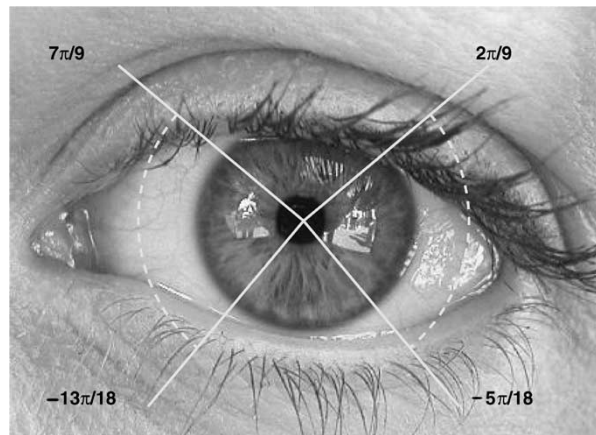


Fig. 3. Cropped image of the eye with two initial limbus sectors superimposed. The initial origin  $(x_0^{(0)}, y_0^{(0)})$  is determined by the QSI detector.

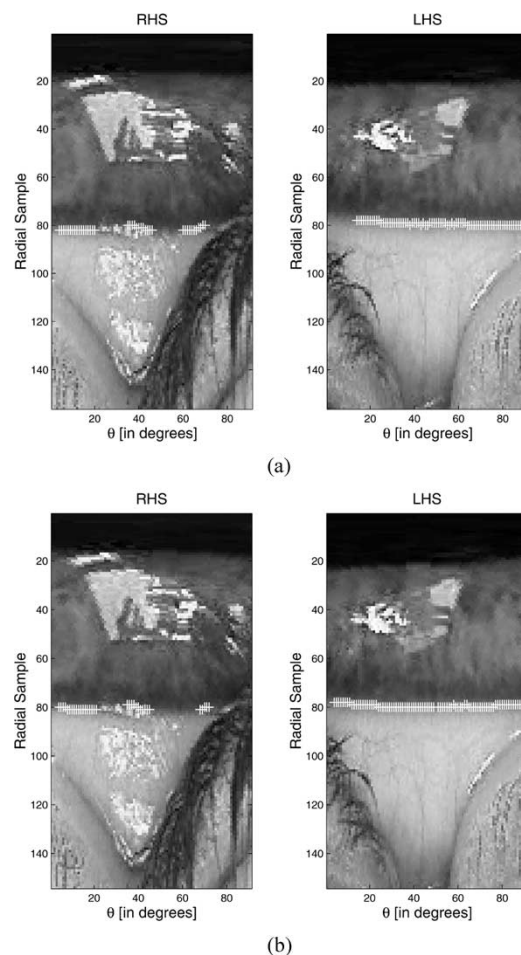


Fig. 4. The right- and left-hand side limbus sectors transformed from Cartesian to polar coordinates at iteration (a)  $i = 0$  and (b)  $i = 1$ . The detected points of the limbus outline are indicated by white crosses, at values of approximately 80 on the  $y$  axis.

iris area to the white sclera. Then, a gradient-based algorithm is used to find the location of this transition for the average profile in the first instance and subsequently for all individual radial profiles. The mathematical formulation of the proposed detection procedure is given in Section III.

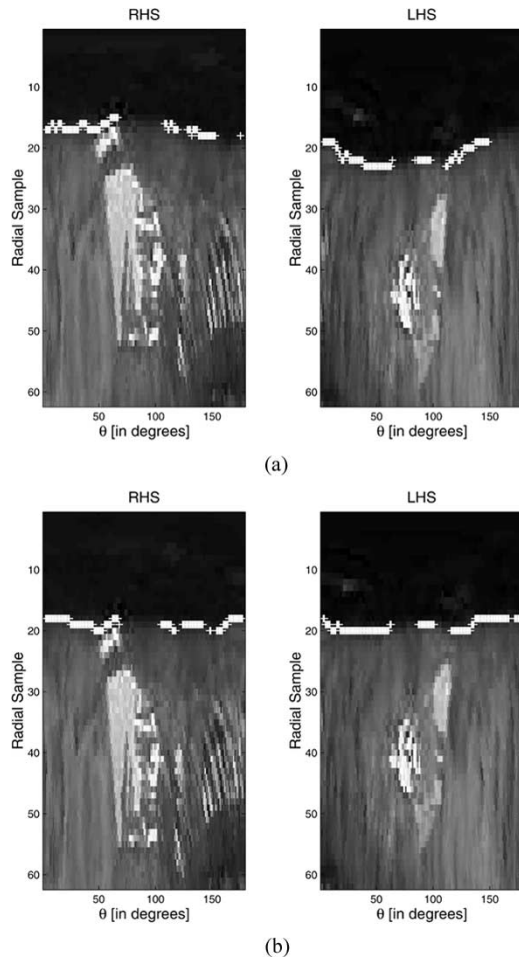


Fig. 5. The right and left-hand side pupil sectors transformed from Cartesian to polar coordinates at iteration (a)  $k = 0$  and (b)  $k = 1$ . The detected points of pupil outline are indicated by white crosses, at values of approximately 20 on the  $y$  axis.

The detected candidate points of the corneal limbus are used to estimate the parameters of the limbus model. For most applications, modeling the limbus outline with a circle or an ellipse is sufficient [22], [33]. The estimated center of the limbus is then used as the new origin and a new set of limbus sectors is accordingly selected. The procedure of detecting and estimating limbus parameters is then repeated until the Euclidean distance between the origins at two consecutive iterations reaches a preset threshold  $T$ .

The pupil parameters can be estimated in a similar manner. First, a set of initial pupil sectors need to be selected. For most images, the pupil sectors will cover the whole pupil area (i.e., from 0 to  $2\pi$  or more specifically from  $-\pi/2$  to  $\pi/2$  for the right-hand side sector and from  $\pi/2$  to  $-\pi/2$  for the left-hand side sector). However, when the eyelids partially obstruct the pupil area the pupil sectors must be changed. This is particularly important when estimating pupil parameters during an eyeblink. In Section IV, we discuss this issue in more detail. After initial pupil sectors are chosen a transformation from Cartesian to polar coordinates is performed as shown in Fig. 5. In this case, however, the radial distance in the sampling procedure is restricted to about 80% of the estimated iris diameter.

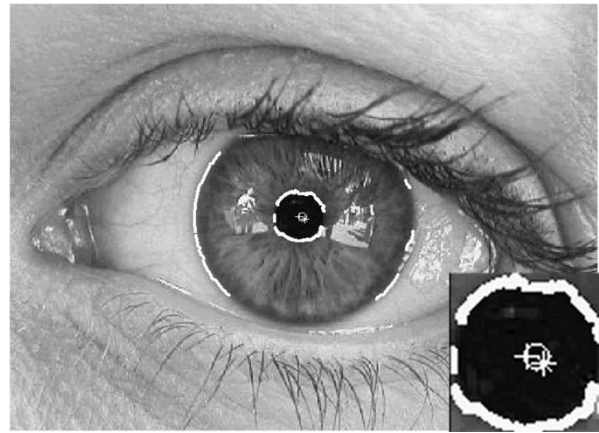


Fig. 6. The image of the eye with superimposed limbus and pupil candidate points and the estimated centers of the eye. The initial eye center (via QSI) is indicated by a circle, the limbus center by a star, and the pupil center by a cross (see inset image).

The procedure for detecting pupil outline is similar to that of limbus extraction. Again, we first average the radial profiles over the pupil sector to estimate the trend in the intensity. It is expected that the average pupil profile has a clear transition from the dark pupil area to the higher intensity iris area. For eyes with very dark irides, this transition may not be clear. One solution to this problem is to use infrared light for illumination and enhance this transition. The location of the pupil outline is achieved by a gradient-based algorithm. As in the case of the limbus, we first find the transition for the average profile and then for all individual radial profiles. Section III provides details of this procedure.

Several parametric models exist for pupil shape. For most clinical applications, the use of a circle or an ellipse is sufficient. However, for more detailed analysis, a finite Fourier series can be used [24]. After parameter estimation is performed, the center of the pupil is estimated. This is achieved by either choosing the center of the best fit circle or the center of the pupil mass. Then, a new origin is set to form a new set of pupil sectors. The detection and estimation procedures are iterated as in the case of the limbus until the Euclidean distance between the origins at two consecutive iteration reaches a preset threshold  $T$ .

In Fig. 6, we show the result of the detection of pupil and limbus outlines after the procedure is finalized. The initial center of the eye detected with the QSI is indicated by a white circle, the limbus center by a star, and the pupil center by a cross (see inset image). Fig. 7 shows the image of the eye with superimposed circular estimates of the pupil and limbus outlines. In Section III, we provide the mathematical details of the proposed procedure.

### III. DETECTION AND ESTIMATION

As indicated in Fig. 1, the part of the procedure that detects the limbus outline is almost identical to that for pupil extraction. Note, however, that the two algorithms are not performed simultaneously. In the following, we will first describe in detail the detection and estimation steps for the case of the limbus.

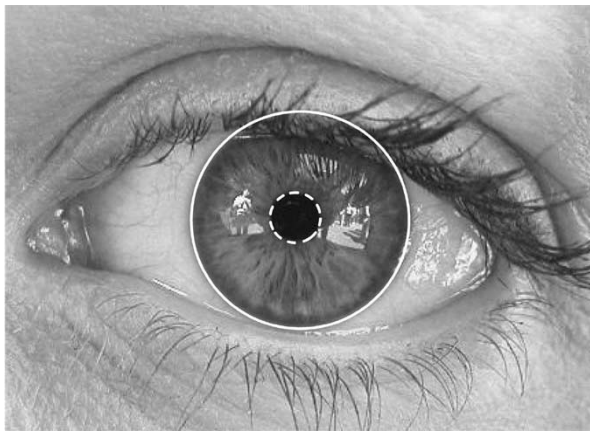


Fig. 7. The image of the eye with superimposed estimated limbus (solid line) and pupil outlines (dashed line).

This is followed by general remarks regarding the differences in the methodology that need to be taken into account when extracting pupil information.

#### A. Limbus Extraction

Let  $I(x, y)$ ,  $x = 1, \dots, n_x$ , and  $y = 1, \dots, n_y$  be the intensity of a gray-scale image, where  $n_x$  and  $n_y$  denote the number of pixels in the image in the  $x$  and  $y$  directions, respectively. From now on we will refer to  $I(x, y)$  as an image.

First, we set the limbus iteration counter  $i$  to zero and choose the initial origin  $(x_0^{(i)}, y_0^{(i)})$  by using the QSI-based detector [30] or simply by selecting the center of the image, i.e.,  $x_0^{(i)} = \lfloor n_x/2 \rfloor$  and  $y_0^{(i)} = \lfloor n_y/2 \rfloor$ , where  $\lfloor \cdot \rfloor$  denotes the floor operator. In the latter case, care should be taken to ensure that the initial origin lies within the pupil or iris areas. Next, we select the initial angular range for the limbus sectors for the right-hand  $(\theta_{\min}^{(i, \text{RHS})}, \theta_{\max}^{(i, \text{RHS})})$  and left-hand  $(\theta_{\min}^{(i, \text{LHS})}, \theta_{\max}^{(i, \text{LHS})})$  sides of the image as well as the maximum radius  $r_{\max} = \min[x_0^{(i)}, y_0^{(i)}]$  of a circle inscribed in the image  $I(x, y)$  and centered on  $(x_0^{(i)}, y_0^{(i)})$ . For clarity of presentation, we will omit the superscripts RHS and LHS and return to them only when they are essential.

Several methods exist that allow us to transform an image from the Cartesian to polar coordinates [22], [34]. Typically, a set of equidistant concentric rings is chosen to which uniform angular sampling is applied (samples taken at zeros of an angular harmonic function). Alternatively, one may choose sampling at points that are roots of another function such as the Bessel  $J_0$  function [35]. Since the transformation from the Cartesian to polar coordinates is not critical in our application, we choose a zero-order (nearest neighbor) interpolation at a basic concentric grid where the radial rings are spaced one pixel

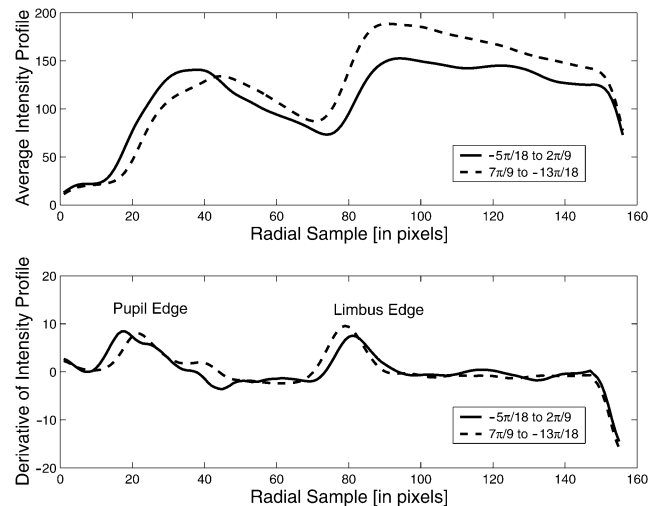


Fig. 8. Averaged intensity profiles (top) and their derivatives (bottom) for the RHS (solid lines) and LHS (dashed lines) limbus sectors at iteration  $i = 0$ .

apart and the angular samples are taken at equidistant angular steps.

Thus, for each limbus sector, we define a radial image profile  $I_p(r, \theta)$ ,  $r = 1, \dots, r_{\max}$ ,  $\theta = \theta_{\min}, \theta_{\min} + \delta\theta, \theta_{\min} + 2\delta\theta, \dots, \theta_{\max}$ , where  $\delta\theta$  is a predetermined angular step. We can then form an  $n_r \times n_\theta$  polar-grid matrix with columns corresponding to sampled radial profiles

$$I_p = \begin{bmatrix} I_p(1, \theta_{\min}) & \dots & I_p(1, \theta_{\max}) \\ I_p(2, \theta_{\min}) & \dots & I_p(2, \theta_{\max}) \\ \vdots & \vdots & \vdots \\ I_p(r_{\max}, \theta_{\min}) & \dots & I_p(r_{\max}, \theta_{\max}) \end{bmatrix}$$

where  $n_r = r_{\max}$  and  $n_\theta = (\theta_{\max} - \theta_{\min})/\delta\theta + 1$ . An example of limbus sector matrices is shown in Fig. 4. To detect the limbus outline, we first find the average radial intensity, as shown in the equation at the bottom of the page, where  $r = 1, \dots, r_{\max}$ , which is further smoothed with a Gaussian kernel to remove local noise such as reflections in the iris. Fig. 8 (top) shows an example of average intensity profiles for the image of an eye. We note that for both the right and left-hand side limbus sectors there are two quick transitions in the intensity profile. The first transition corresponds to the pupil outline while the second one to the limbus outline. These two transitions can be easily detected by calculating the average intensity gradient

$$\gamma_p(q) = \tilde{I}_p(q) - \tilde{I}_p(q-1), \quad q = 2, \dots, r_{\max}$$

and searching for the strongest local maxima as shown at the bottom of Fig. 8. We note that the maxima in the right and left-hand side limbus sectors are not at the same radial distance from the origin. This means that the initial origin  $(x_0^{(0)}, y_0^{(0)})$  does not coincide with the center of the limbus and the procedure needs to be reiterated.

$$\bar{I}_p = \frac{1}{n_\theta} \begin{bmatrix} \sum_{\theta=\theta_{\min}}^{\theta_{\max}} I_p(1, \theta) & \sum_{\theta=\theta_{\min}}^{\theta_{\max}} I_p(2, \theta) & \dots & \sum_{\theta=\theta_{\min}}^{\theta_{\max}} I_p(r_{\max}, \theta) \end{bmatrix}' = \bar{I}_p(r)$$

Before we proceed any further, we need to define certain characteristic features in the image radial intensity profile. We are interested in extracting the two strongest maxima in the gradient of the intensity profile. This can be achieved by calculating the second derivative of the radial intensity profile and using a zero-crossing technique. The first peak in the decreasing order of the radial sample  $r$  corresponds to the average limbus edge, which we denote by  $\gamma_{\max_L}$ . Similarly the second peak corresponds to the average pupil edge, though this characteristic is not of interest in this particular step of the procedure. We will return to the pupil edge characterization later.

Next, let us define the average limbus band as the difference between the left and the right-hand side average limbus edges, i.e.,

$$B_L = |\gamma_{\max_L}^{\text{LHS}} - \gamma_{\max_L}^{\text{RHS}}|.$$

To detect the limbus outline, the following approach is used. Essentially, for each of the radial profiles,  $I_p(r, \theta_{\min}), \dots, I_p(r, \theta_{\max})$ , we smooth the data with a Gaussian kernel, calculate the derivative, find the local limbus edge, and test it against the  $\gamma_{\max_L}$ . However, it has been observed that smoothing (averaging) is also necessary in the angular direction. Thus, we decide to run an angular mask  $M$  of size  $n_M < n_\theta$  across the extracted portion of angular data, and each time calculate the average limbus edge as outlined above. The decision of inclusion depends on whether the local estimate of the limbus edge lies within the average band  $B_L$  centered on  $\gamma_{\max_L}$ . A more rigorous hypothesis testing procedure could be employed. However, the feasibility of such an approach is questionable taking into account that the distribution of the test statistic under the null hypothesis is usually unknown.

In the next step, the detected candidate points of the limbus outline are used to estimate the parameters of a limbus model. As mentioned in Section II, fitting a circle or an ellipse to the limbus is typically sufficient from a clinical point of view. In the case of the ellipse we use a 5-parameter model described by the following equation:

$$\begin{aligned} & \{r \cos \theta - x_c\}^2 \zeta_1(p, \phi) \\ & + 2\{r \cos \theta - x_c\}\{r \sin \theta - y_c\} \zeta_2(p, \phi) \\ & + \{r \sin \theta - y_c\}^2 \zeta_3(p, \phi) - b^2 = 0 \end{aligned} \quad (1)$$

where

$$\begin{aligned} \zeta_1(p, \phi) &= p \cos^2(\phi) + \sin^2(\phi) \\ \zeta_2(p, \phi) &= \cos(\phi) \sin(\phi) (1 - p) \\ \zeta_3(p, \phi) &= p \sin^2(\phi) + \cos^2(\phi) \end{aligned}$$

and  $p = b^2/a^2$ .  $(x_c, y_c)$  is the ellipse center,  $\phi$  determines the angular rotation while  $2a$  and  $2b$  are the two principal axes in the  $\phi$  and  $\phi + \pi/2$  directions, respectively. A linear in parameters least square procedure for estimating the parameters of model (1) is given in [22].

The estimated limbus center  $(\hat{x}_c^{(i)}, \hat{y}_c^{(i)})$  at iteration  $i$  becomes the location of the new origin, i.e.,

$$x_0^{(i+1)} = \hat{x}_c^{(i)} \text{ and } y_0^{(i+1)} = \hat{y}_c^{(i)}.$$

The procedure of setting the limbus sectors, detection and estimation is then repeated until the Euclidean distance between the origins at two consecutive iterations satisfies

$$E(i) = \sqrt{(x_0^{(i)} - x_0^{(i-1)})^2 + (y_0^{(i)} - y_0^{(i-1)})^2} \leq T$$

where  $T$  is predetermined threshold often set to zero.

One may ask whether the algorithm is guaranteed to converge. Deriving a mathematical proof for the algorithm's convergence is not feasible for the range of images encountered in clinical practice. Our practical experience with hundreds of images has shown that for most of them the algorithm converges after three iterations. However, the algorithm could diverge if the initial estimator of the pupil center, performed with the QSI detector, lies outside the pupil area. In such cases, the algorithm is stopped and an operator is asked to manually adjust the initial pupil center.

### B. Pupil Extraction

As mentioned earlier, the procedure of extracting the pupil outline is analogous to what we have described for detecting the limbus. The main differences are outlined below.

- 1) The radial sampling is bounded to about 80% of the limbus edge  $\gamma_{\max_L}$ . However, this ratio may need to be changed for some pathological cases.
  - 2) The pupil sectors,  $(\theta_{\min}^{(k, \text{RHS})}, \theta_{\max}^{(k, \text{RHS})})$  and  $(\theta_{\min}^{(k, \text{LHS})}, \theta_{\max}^{(k, \text{LHS})})$  are selected independently to limbus sectors.
  - 3) The algorithm for pupil extraction is iterated independently; hence, the superscript  $(k)$  in the pupil sectors above.
  - 4) The pupil sectors form a new polar-grid matrix of size  $N_r \times N_\theta$  where  $N_r = \lfloor 0.8\gamma_{\max_L} \rfloor$  and  $N_\theta = \lfloor (\theta_{\max} - \theta_{\min}) / \delta_\theta \rfloor$ . An example of polar sector matrices is shown in Fig. 5.
- We note that at the first iteration,  $k = 0$  the detected points do not form a straight line, which clearly indicates that the center of limbus does not coincide with the center of pupil. This is quickly rectified in the second iteration  $k = 1$ , as shown in Fig. 5(b). As in the case of the limbus, the procedure converges within several iterations for most images.
- 5) After selecting the candidate points, a parametric pupil model is applied. Again a circle or an ellipse provide a good estimate. However, in clinical studies where the noncircularity of the pupil is of interest a finite Fourier series is used.

The output of the pupillometry procedure consists of a set of pupil and limbus parameters including pupil/limbus sizes and centers.

## IV. APPLICATIONS

In the following, we show two applications of the proposed procedure. First we use images from a pupil viewer of a wavefront sensor. Next, we apply our algorithm to a high-speed imaging system.

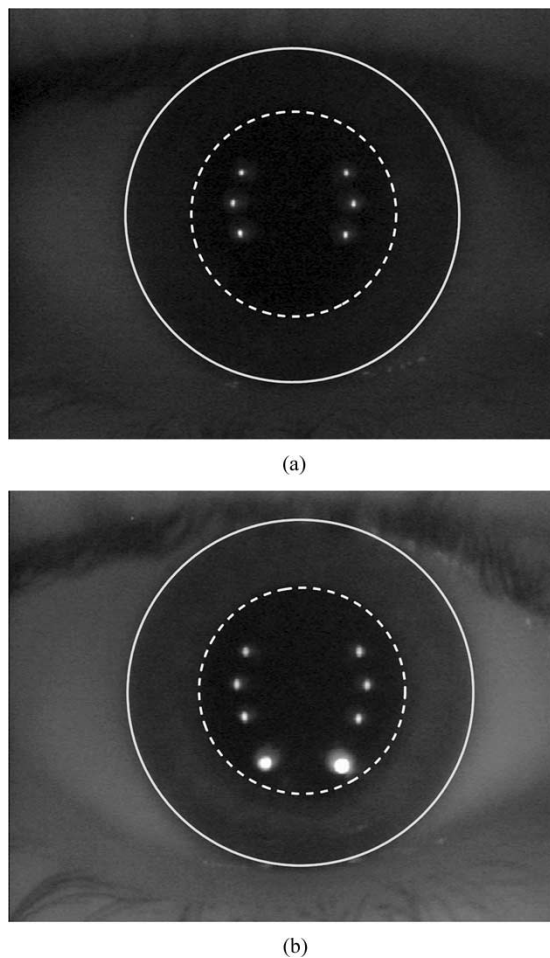


Fig. 9. An example of images from the pupil viewer of the wavefront sensor with the estimated pupil (dashed line) and limbus (solid line) outlines. (a) Image acquired with original instrument setting. (b) Image with additional illumination.

#### A. Wavefront Sensing

A Hartmann–Shack sensor is used to measure the optical aberrations of the eye [36]. It is equipped with a laser, an array of small lenses, and an imaging device. The monochromatic light reflected from the retina and passing through the array of lenses forms the image that is captured with a CCD camera. This image is used to calculate the wavefront aberrations of the eye. An additional CCD camera is used as the pupil viewer.

Since the measurement of the wavefront aberration is often performed in scotopic conditions, it is of interest to relate the measurement back to that of the photopic condition. However, the pupil size and center changes and the only way to control this is to measure these two parameters relative to the limbus outline. We use the image from the pupil viewer for this task. An example of the wavefront sensor image<sup>1</sup> of the pupil is shown in Fig. 9(a). The reflections in the pupil are from the six light-emitting diodes (LED) that are used for targeting. The position of the LEDs are known *a priori* and can be excluded from the analysis in the algorithm. We note that despite the very low intensity of the image, the algorithm can successfully detect the limbus and pupil outlines. We used default settings for the limbus and pupil sectors as outlined in Section II.

<sup>1</sup>COAST™, Wavefront Sciences, Inc.

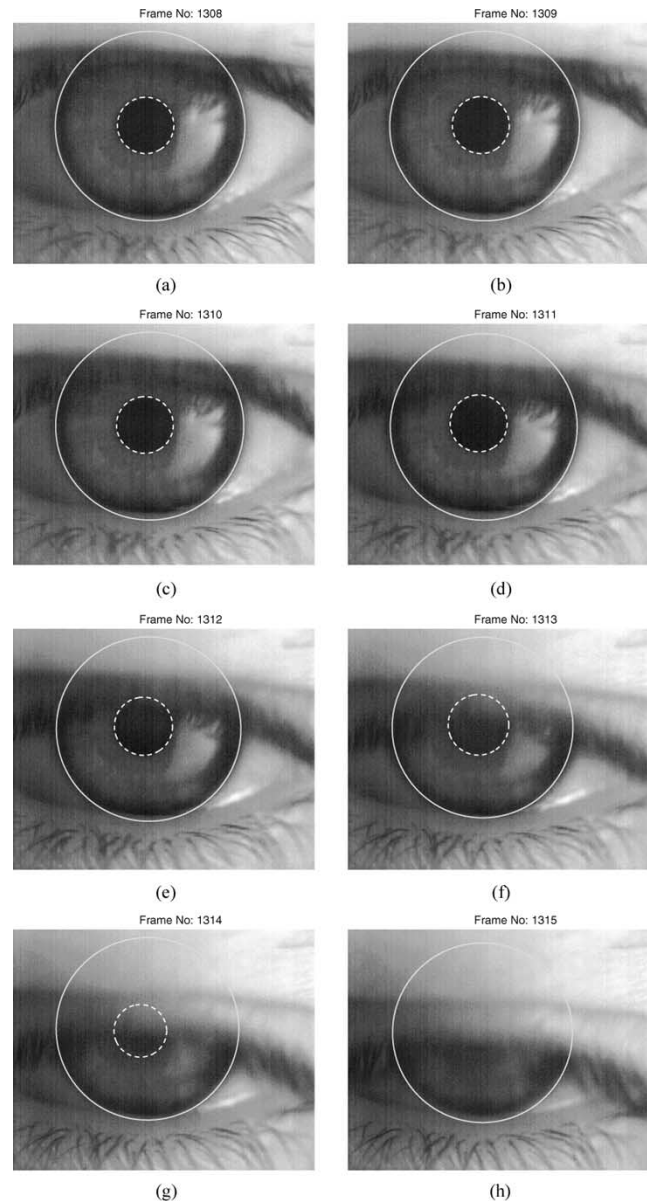


Fig. 10. An example of eight consecutive frames taken during the first phase of the blink with the estimated pupil (dashed line) and limbus (solid line) outlines. The sampling rate was set to 250 fps.

We have experimented with additional illumination achieved by two red LEDs placed at the front of the instrument. In Fig. 9(b) we show the result of finding the pupil and limbus outlines in such a scenario. For this particular image we have adjusted the pupil sectors to avoid reflections from the additional LEDs. Specifically, we have set the right-hand sector between  $-5\pi/18$  and  $\pi/2$  and left-hand sector between  $\pi/2$  and  $-13\pi/18$ . The examples given show the versatility of the proposed method.

#### B. High-Speed Imaging

To assess the dynamic changes in pupil size and centration, we used a high-speed camera (Redlake MotionPro) with  $1280 \times 1204$  pixels. The sampling rate was set to 250 frames per second (fps). Since it is a CMOS camera, it requires significant light for the images to be captured. For this reason,

we used a powerful 300-W back light that has been diffused by reflection from a white board. An example of eight consecutive frames (4 ms apart) taken during the first phase of the blink is shown in Fig. 10. Note the irregular illumination, reflection of the white board in the iris, and very narrow depth of focus.

We have applied the procedure outlined in Sections II and III to the images acquired with a high-speed camera. As noted in Fig. 1, in such a case we may need to change the initial limbus and pupil sectors. The adjustment of those sectors was not necessary for the first four frames [see Fig. 10(a)–(d)]. When the amount of the detected candidate points started to diminish for subsequent frames, both the limbus and pupil sectors had to be adjusted. Currently, this step of the procedure is not fully automatic and depends largely on the position of the eyelids during the blink.

The proposed procedure performed well. However, when the pupil becomes too obscured by the eyelids, the algorithm overestimates [Fig. 10(f)] or underestimates [Fig. 10(g)] the true pupil size. Despite this drawback, the algorithm is able to provide vision researchers with information on the pupil dynamics that was unavailable in the past.

## V. CONCLUSION

We have developed a robust algorithm for estimating pupil parameters from a variety of digital images. Unlike its predecessors, the technique is able to relate the pupil position to the limbus which can be considered a constant feature of the eye. In the past, this type of analysis was performed manually.

The procedure utilizes gradient-based algorithms. This may suggest that the procedure can be further improved by applying more advanced edge detection techniques. This might be the case if the technique was used for relatively uniform input images. However, our experience shows that every human eye has unique features which are often hard to generalize. Also, it is difficult to control the image acquisition protocol when different instrumentation in a range of lighting conditions is used.

There are other limitations of the procedure. Although for most clinical images there is no need to adjust limbus sectors and the procedure is fully automatic, manual selection of the sectors is necessary for full left and right gazes or when studying the pupil during blinking. The latest issue has been recently addressed in [37] where a procedure for extracting eyelid position relevant to the limbus was proposed.

The purpose of this paper was to introduce the methodology of automatic pupillometry and show its robustness. Clinical studies that use the proposed technique are being conducted and their results will be reported elsewhere.

## REFERENCES

- [1] G. Walsh and W. N. Charman, "The effect of pupil centration and diameter on ocular performance," *Vis. Res.*, vol. 28, pp. 659–665, 1988.
- [2] G. Walsh, "The effect of mydriasis on the pupillary centration of the human eye," *Ophthalm. Physiol. Opt.*, vol. 8, no. 4, pp. 178–182, 1988.
- [3] A. M. Fay, S. L. Trokel, and J. A. Myers, "Pupil diameter and the principal ray," *J. Cataract Refract. Surg.*, vol. 18, no. 7, pp. 348–351, 1992.
- [4] M. A. Wilson, M. C. W. Campbell, and P. Simonet, "Change of pupil centration with change of illumination and pupil size," *Optom. Vis. Sci.*, vol. 69, no. 2, pp. 129–136, 1992.
- [5] M. Pande and J. S. Hillman, "Optical zone centration in keratorefractive surgery," *Ophthalmology*, vol. 100, no. 8, pp. 1230–1237, 1993.
- [6] J. T. Holladay, "The high cost of inaccurate pupillometry," *Rev. Ophthalmol.*, vol. 9, no. 3, pp. 47–49, 2002.
- [7] E. S. Rosen, C. L. Gore, D. Taylor, D. Chitkara, F. Howes, and E. Kowalewski, "Use of a digital infrared pupillometer to assess patient suitability for refractive surgery," *J. Cataract Refract. Surg.*, vol. 28, no. 8, pp. 1433–1438, 2002.
- [8] J. Schwiegerling and R. W. Snyder, "Eye movement during laser in situ keratomileusis," *J. Cataract Refract. Surg.*, vol. 26, no. 3, pp. 345–351, 2000.
- [9] M. Mrochen, M. S. Eldine, M. Kaemmerer, T. Seiler, and W. Hütz, "Improvement in photorefractive corneal laser surgery results using an active eye-tracking system," *J. Cataract Refract. Surg.*, vol. 27, no. 7, pp. 1000–1006, 2001.
- [10] J. W. McLaren, P. J. Hauri, S.-C. Lin, and C. D. Harris, "Pupillometry in clinically sleepy patients," *Sleep Medicine*, vol. 3, pp. 347–352, 2002.
- [11] K. Fountoulakis, F. Fotiou, A. Iacovides, J. Tsiptsios, A. Goulas, M. Tsolaki, and C. Ierodiakonou, "Changes in pupil reaction to light in melancholic patients," *Int. J. Psychophysiol.*, vol. 31, pp. 121–128, 1999.
- [12] M. M. Stark, K. Englehart, B. F. Sexton, R. Tunbridge, and P. Jackson, "Use of a pupillometer to assess change in pupillary size post-cannabis," *J. Clin. Forensic Med.*, vol. 10, pp. 9–11, 2003.
- [13] R. B. Mandell, C. S. Chiang, and S. A. Klein, "Location of major corneal reference points," *Optom. Vis. Sci.*, vol. 72, no. 11, pp. 776–784, 1995.
- [14] I. Karpouzias and Y. Poulouken, "Modeling and numerical optimization of corneal rotation," *IMA J. Math. Appl. Med. Biol.*, vol. 8, pp. 73–82, 1991.
- [15] A. Langenbacher, B. Seitz, M. M. Kus, E. Vilchis, and G. O. H. Naumann, "Graft decentration in penetrating keratoplasty: Nonmechanical trephination with the excimer laser (193 nm) versus the motor trephine," *Ophthalm. Surg. and Lasers*, vol. 29, no. 2, pp. 106–113, 1998.
- [16] H. Obstfeld and B. R. Chou, "A study of the accuracy of corneal reflection pupillometers," *Ophthalm. Physiol. Opt.*, vol. 18, no. 6, pp. 527–531, 1998.
- [17] E.-M. Schnitzer, M. Baumeister, and T. Kohnen, "Scotopic measurement of normal pupils: Colvard versus video vision analyzer infrared pupillometer," *J. Cataract Refract. Surg.*, vol. 26, no. 6, pp. 859–866, 2000.
- [18] M. Pop, Y. Payette, and E. Santoriello, "Comparison of the pupil card and pupillometer in measuring pupil size," *J. Cataract Refract. Surg.*, vol. 28, no. 2, pp. 283–288, 2002.
- [19] T. Kohnen, E. Terzi, J. Bühren, and E.-M. Kohnen, "Comparison of a digital and a handheld infrared pupillometer for determining scotopic pupil diameter," *J. Cataract Refract. Surg.*, vol. 29, no. 1, pp. 112–117, 2003.
- [20] B. S. B. Wachler and R. R. Krueger, "Agreement and repeatability of pupillometry using videokeratography and infrared devices," *J. Cataract Refract. Surg.*, vol. 26, no. 1, pp. 35–40, 2000.
- [21] R. Fogla and S. K. Rao, "Pupillometry using videokeratography in eyes with dark brown irides," *J. Cataract Refract. Surg.*, vol. 26, no. 9, pp. 1266–1267, 2000.
- [22] M. R. Morelande, D. R. Iskander, M. J. Collins, and R. Franklin, "Automatic estimation of corneal limbus in videokeratoscopy," *IEEE Trans. Biomed. Eng.*, vol. 49, pp. 1617–1625, Dec. 2002.
- [23] Y. Yang, K. Thompson, and S. Burns, "Pupil location under mesopic, photopic, and pharmacologically dilated conditions," *Investigat. Ophthalmol. Vis. Sci.*, vol. 43, no. 7, pp. 2508–2512, 2002.
- [24] H. J. Wyatt, "The form of the human pupil," *Vis. Res.*, vol. 35, no. 14, pp. 2021–2036, 1995.
- [25] R. C. Gonzalez and R. E. Woods, *Digital Image Processing*, 2nd ed. Englewood Cliffs, NJ: Prentice-Hall, 2002.
- [26] J.-G. Wang and E. Sung, "Study on eye gaze estimation," *IEEE Trans. Syst., Man, Cybern. B*, vol. 32, pp. 332–350, Mar. 2002.
- [27] P.-K. Ser and W.-C. Siu, "Novel detection of conics using 2-D hough planes," *Proc. Inst. Elect. Eng.—Vision, Image and Signal Processing*, vol. 142, no. 5, pp. 262–270.
- [28] J. C. Barry, U. M. Pongs, and W. Hillen, "Algorithm for Purkinje images I and IV and limbus centre localization," *Comput. Biol. Medicine*, vol. 27, no. 6, pp. 515–531, 1997.
- [29] I. Miro, N. Lopez-Gil, and P. Artal, "Pupil-meter and tracking system based in a fast image processing algorithm," *Proc. SPIE*, vol. 3591, pp. 63–70, 1999.
- [30] D. R. Iskander, S. Mioschek, M. Trunk, and W. Werth, "Detecting eyes in digital images," in *Proc. 7th Int. Symp. Signal Processing and its Applications*, vol. II, Paris, France, July 2003, pp. 21–24.
- [31] C. H. Morimoto, D. Koons, A. Amir, and M. Flickner, "Pupil detection and tracking using multiple light sources," *Image Vis. Comput.*, vol. 18, pp. 331–335, 2000.

- [32] D. Zhu, S. T. Moore, and T. Raphan, "Robust pupil centre detection using a curvature algorithm," *Comput. Methods and Programs in Biomed.*, vol. 59, pp. 145–157, 1999.
- [33] R. B. Mandell, "A guide to videokeratography," *Int. Contact Lens Clinic*, vol. 23, no. 6, pp. 205–228, 1996.
- [34] W. Lawton, "A new polar Fourier transform for computer-aided tomography and spotlight synthetic aperture radar," *IEEE Trans. Acoust., Speech, Signal Processing*, vol. 36, pp. 931–933, June 1988.
- [35] N. Myrdis and C. Chamzas, "Sampling on concentric circles," *IEEE Trans. Med. Imag.*, vol. 17, pp. 294–299, Apr. 1998.
- [36] J. Liang, B. Grimm, S. Goelz, and J. F. Bille, "Objective measurement of wave aberrations of the human eye with the use of a Hartmann-Shack wave-front sensor," *J. Opt. Soc. Amer. A*, vol. 11, no. 7, pp. 1949–1957, 1994.
- [37] S. S. S. Phang, D. R. Iskander, and M. J. Collins, "High speed pupillometry," in *Proc. 8th Australian and New Zealand Intelligent Information Systems Conf. (ANZIS 2003)*, Sydney, Australia, Dec. 2003, pp. 43–47.



**D. Robert Iskander** (M'98) received the M. Ing. degree in electronic engineering from the Technical University of Lodz, Lodz, Poland, in 1991, and the Ph.D. degree in signal processing from Queensland University of Technology (QUT), Brisbane, Australia, in 1997.

From 1996 to 2000, he was a Research Fellow at the Signal Processing Research Centre, the Cooperative Research Centre for Satellite Systems, and the Centre for Eye Research, QUT. In 2001, he joined the School of Engineering, Griffith University, as a Senior Lecturer. In July 2003, he returned to the Centre for Health Research (Optometry) as a Principal Research Fellow. He is also an Honorary Fellow at Griffith University. His current research interests include statistical signal processing, visual optics and optometry.

Dr. Iskander is a member of the Association for Research in Vision and Ophthalmology.



**Michael J. Collins** received the Dipl. Appl. Sci. in optometry, and the M. Appl. Sci. and Ph.D. degrees from Queensland University of Technology, Brisbane, Australia, in 1977, 1988, and 1996, respectively.

He is an Associate Professor in the School of Optometry, Queensland University of Technology. His research laboratory, the Contact Lens and Visual Optics Laboratory, specializes in the visual and optical characteristics of the cornea and contact lenses.

Dr. Collins is a member of the Optometrists Association of Australia and a Fellow of the American Academy of Optometry and the Contact Lens Society of Australia.



**Siegfried Mioschek** received the Dipl. Ing. degree in electronic engineering from the School of Electronics, Carinthia Tech Institute, Austria, in 2003.

In 2002, he joined the Contact Lens and Visual Optics Laboratory, Queensland University of Technology, Brisbane, Australia, as a Visiting Research Student. His interest include control systems and image processing.



**Martin Trunk** (M'03) received the Dipl. Ing. degree in electronic engineering from the School of Electronics, Carinthia Tech Institute, Villach, Austria, in 2003.

In 2002, he joined the Contact Lens and Visual Optics Laboratory, Queensland University of Technology, Brisbane, Australia, as a Visiting Research Student. Currently, he is with Byometric Systems GmbH, Mitterfelden, Germany. His interests include image processing and biometrics.